

Plastic Morphological Response to Spectral Shifts during Inorganic Phototropic Growth

Kathryn R. Hamann, Madeline C. Meier, Nathan S. Lewis,* and Azhar I. Carim*

Cite This: *JACS Au* 2022, 2, 865–874

Read Online

ACCESS |

Metrics & More

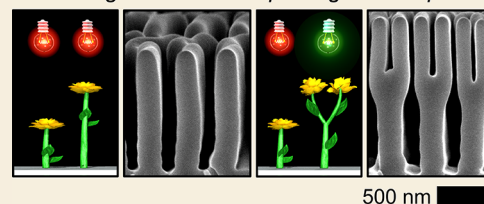
Article Recommendations

Supporting Information

ABSTRACT: Plants exhibit phototropism in which growth is directed toward sunlight and demonstrate morphological plasticity in response to changes in the spectral distribution of the incident illumination. Inorganic phototropic growth via template-free, light-directed electrochemical deposition of semiconductor material can spontaneously generate highly ordered mesostructures with anisotropic, nanoscale lamellar features that exhibit a pitch proportional to the wavelength (λ) of the stimulating illumination. In this work, Se–Te films were generated via a two-step inorganic phototropic growth process using a series of narrowband light-emitting diode sources with discrete output wavelengths ($\lambda_0 \neq \lambda_1$). Analogous to the plasticity observed in plants, changes in illumination wavelength from λ_0 to λ_1 resulted in morphological changes including feature branching, termination, and/or fusion along the growth direction. The interfacial feature pitch changed with the growth duration, in some cases in a notably nonmonotonic fashion, and eventually matched that obtained for growth using only λ_1 . Simulated morphologies generated by modeling light–material interactions at the growth interface closely matched the evolved structures observed experimentally, indicating that the characteristics of the optical stimulation produce the observed plastic response during inorganic phototropic growth. Examination of the interfacial electric field modulation for λ_1 illumination of simplified structures, representative of those generated experimentally, revealed the interfacial light scattering and concentration behavior that directed phototropic growth away from equilibrium, as well as the emergent nature of the phenomena that reestablish equilibrium.

KEYWORDS: photoelectrodeposition, photoelectrochemistry, mesostructure, template-free, maskless, optical

Wavelength Directs Morphological Response



Biological systems demonstrate phenotypic plasticity whereby an organism expresses different phenotypes in response to changes in the local environment.¹ This biological plasticity concept encompasses a wide set of responsive phenomena beyond the physics and materials science definition of plasticity that specifically describes a change in the shape of a material as a result of an applied force. Biological plasticity provides for the exhibition of a diversity of morphologies, among other properties, and thus enables an organism to maximize fitness in variable environments. Plants exhibit phenotypic plasticity to compensate in part for the intrinsic inability to move physically to favorable locations.² Moreover, resources that are essential for plant growth are usually distributed heterogeneously within a habitat.³ Plants thus actively control the construction of resource gathering organs, such as root tips and leaves, and are capable of placing these structures nonrandomly to modify the potential for resource acquisition.⁴ Plants are predominantly photosynthetic organisms that depend on sunlight for energy and demonstrate marked morphological plasticity to manage this resource.⁵ The process of phototropism, in which the addition of biomass is directed in a feedback loop to optimize harvesting of solar energy, allows plants to exhibit directed growth in response to illumination.⁶ Cucumber plants, which are shade intolerant, can colonize horizontally patchy environments by preferen-

tially projecting leaf area into light gaps.⁷ In addition to responding to changes in light intensity, plants can display a photomorphogenic response to changes in the spectral distribution of the available illumination. Green plant leaves contain chlorophyll pigment and absorb red light in the ~600 to 700 nm range but transmit and reflect far-red wavelengths in the ~700 to 800 nm regime. The red : far-red intensity ratio of a specific optical stimulus to green leaves provides a metric that enables plants to sense the degree of shading and proximity to neighboring organisms in a specific location.⁵ In response to a diminished red : far-red intensity ratio when overtopped by woody neighbors, open-habitat tree ferns principally produce vertical frond growth.⁸ Increases in the red : far-red intensity ratio provided to geraniums and snapdragons produce photomorphogenesis in which the plant height extension ceases and the leaf area increases.⁹ Thus, the expressed

Received: December 31, 2021

Revised: March 3, 2022

Accepted: March 4, 2022

Published: April 4, 2022



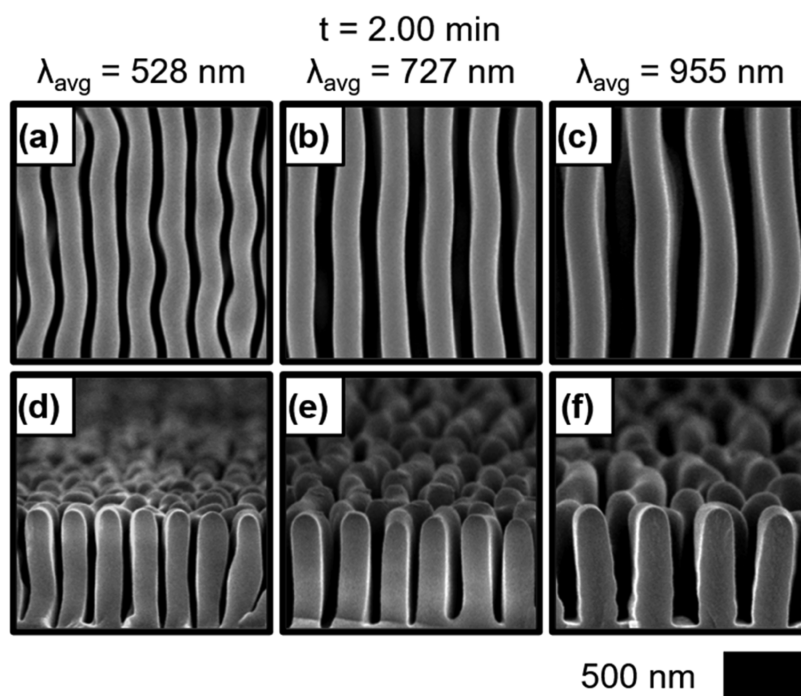


Figure 1. (a–c) Representative top-view and (d–f) cross-sectional SEMs of films generated using the indicated λ_{avg} illumination for $t = 2.00 \text{ min}$.

morphologies of plants are critically dependent on the environmental light conditions.

In analogy to the natural phototropism exhibited by plants, inorganic phototropic growth has been demonstrated in the light-directed electrochemical deposition of chalcogen-based semiconductor materials, including Se–Te, Se–Pb, and Se–Cd.^{10–13} Inorganic phototropic growth produces light-defined mesostructures in which the feature size, orientation, and anisotropies of the morphologies are functions of the input illumination characteristics including the wavelength, polarization, phase, coherence, and direction of the incident illumination.^{10,14–16} Growth using linearly polarized illumination has been demonstrated to generate highly anisotropic and periodic lamellar structures. The long axes of these structures grow parallel to the electric field (E-field) vector of the input illumination and are characterized by a feature pitch (i.e., the distance between nominally identical points on adjacent lamellae) that is proportional to the input wavelength. Analogous to natural phototropism, spatially directed inorganic phototropic growth is a response to local light absorption that promotes local deposition of additional absorber mass. This photoelectrochemical process is compatible with semiconductor materials amenable to solution-phase electrodeposition. Inorganic phototropic growth is modulated by inherent interfacial scattering and absorption processes that define the subwavelength scale distribution of optical field intensity. The evolution of ordered lamellar mesostructures is governed by an emergent, synergistic process in which an individual feature spontaneously scatters the incident illumination and consequently produces spatially anisotropic, concentrated optical intensity at the growth interface of the nearest-neighbor features, promoting asymmetric absorption and addition of new material.¹⁷ Inorganic phototropic growth thus does not require the use of structured light fields, high light intensities, or chemical and physical templating agents because the process exploits inherent optical anisotropies. Moreover, as an emergent process with constituent interactions at the

subwavelength scale, high coherence length sources (e.g., lasers) are not required to produce long-range order. Rather, mesoscale morphologies can be generated over macroscopic areas using light-emitting diode (LED) sources and even broadband incandescent (i.e., heated filament) sources.

Analogous to the growth of plant systems, inorganic phototropic growth has the potential to demonstrate phenotypic plasticity in response to a change in the characteristics of the stimulating illumination. Moreover, such an adaptive growth response may enable straightforward, directed generation of complex three-dimensional morphologies in inorganic films.¹¹ Certain temporal changes in the input wavelength during inorganic phototropic growth can direct mesostructural evolution that results in a new feature pitch at the interface.^{11,18} However, such adaptation may be inhibited by a “history” effect wherein the responsiveness depends not only on the nature of the new optical input but also on the nature of the preexisting structure and thus the prior optical input.¹⁸ This work aims to characterize any plastic morphological responsiveness, with a time-resolved assessment of the transitory growth dynamics including any associated nonlinearities, to a broad series of changes in input wavelength during inorganic phototropic growth. In tandem, this work examines in detail changes in interfacial light scattering and optical field concentration, how these processes mechanistically direct the growth response, and the time-dependent evolution of both phenomena. Here, inorganic phototropic growth was effected via a two-step process that used a series of different LEDs with discrete output wavelengths. The resulting morphologies were evaluated by scanning electron microscopy and Fourier analysis. Modeling of the light-directed deposition and generation of simulated growth morphologies were performed by considering light–material interactions at the growth interface. A comprehensive set of electromagnetic simulations with idealized structure models was then utilized to assess the optical processes that underpin the mechanism of the plastic response.

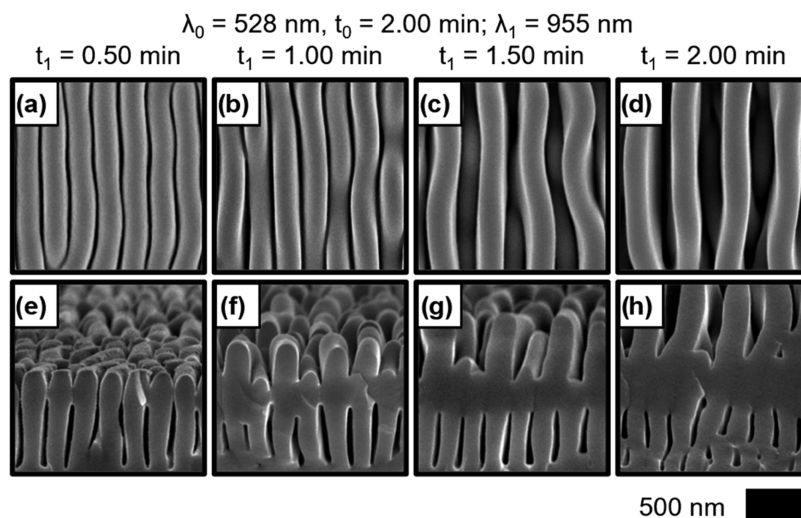


Figure 2. (a–d) Representative top-view and (e–h) cross-sectional SEMs of films generated initially using $\lambda_0 = 528 \text{ nm}$ for $t_0 = 2.00 \text{ min}$ and then extended in a subsequent deposition step using $\lambda_1 = 955 \text{ nm}$ for the indicated t_1 .

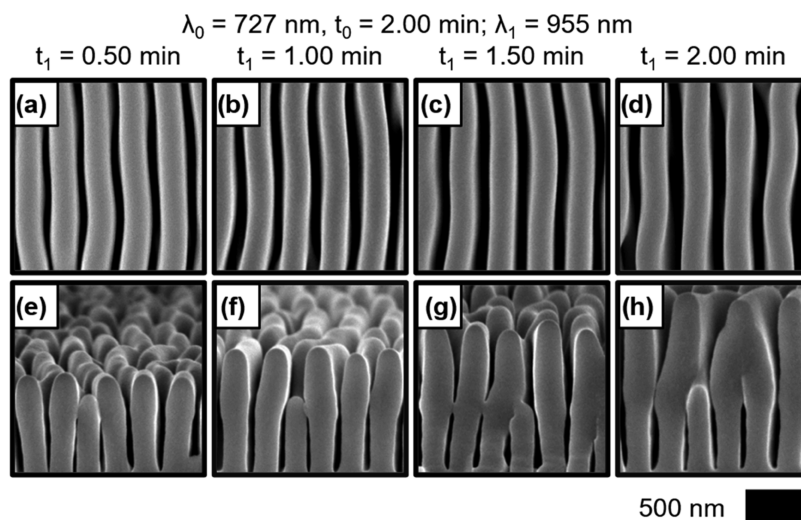


Figure 3. (a–d) Representative top-view and (e–h) cross-sectional SEMs of films generated initially using $\lambda_0 = 727 \text{ nm}$ for $t_0 = 2.00 \text{ min}$ and then extended in a subsequent deposition step using $\lambda_1 = 955 \text{ nm}$ for the indicated t_1 .

RESULTS

Se–Te films were grown from an aqueous solution of oxidized precursors by light-mediated electrodeposition using unstructured, vertically polarized illumination from low-power, narrowband LED sources with values of the intensity-weighted average of the emission spectrum, λ_{avg} , of 528, 727, and 955 nm. The structures produced by deposition for $t = 2.00 \text{ min}$ using these values of λ_{avg} are designated herein as Λ_{528} , Λ_{727} , and Λ_{955} . Se–Te film morphologies were determined using scanning electron microscopy. Figure 1a–c presents representative top-view (from above the sample along the surface normal) scanning electron micrographs (SEMs) of Λ_{528} , Λ_{727} , and Λ_{955} films. Highly anisotropic and periodic lamellar features were observed in which the long axes of the lamellae were oriented vertically, parallel to the input polarization vector. The feature width and feature pitch scaled with λ_{avg} (Figure S1 presents SEMs of Λ_{528} , Λ_{727} , and Λ_{955} films with the pitch denoted graphically). Two-dimensional Fourier transform (2D FT) analysis of top-view SEM data was used to quantify the pitch at the top interface and values of 203 ± 6 ,

263 ± 6 , and $371 \pm 6 \text{ nm}$ were measured for Λ_{528} , Λ_{727} , and Λ_{955} films, respectively; Figure S2 presents a representative set of these 2D FT data. Figure 1d–f presents representative cross-sectional (view perpendicular to the substrate normal) SEMs complementary to the top-view data presented in Figure 1a–c. The cross-sectional analysis was performed by physically cleaving the substrates and top-facing films perpendicular to the direction of the input polarization vector. These cleaved films were then viewed at a near grazing angle to assess the out-of-plane morphology of individual features at single points along the long axes of the lamellae. The cross-sectional SEM data revealed that the features were oriented along a vector normal to the substrate and exhibited substantial anisotropy in this direction. Films generated with extended growth durations using constant illumination at a given wavelength exhibited linear extension of features along the out-of-plane direction but did not exhibit a change in the in-plane morphology (Figure S3). Thus, lamellar mesostructures were characterized by long, anisotropic axes in one in-plane direction, nanoscale feature widths in the orthogonal in-plane direction, and tunable

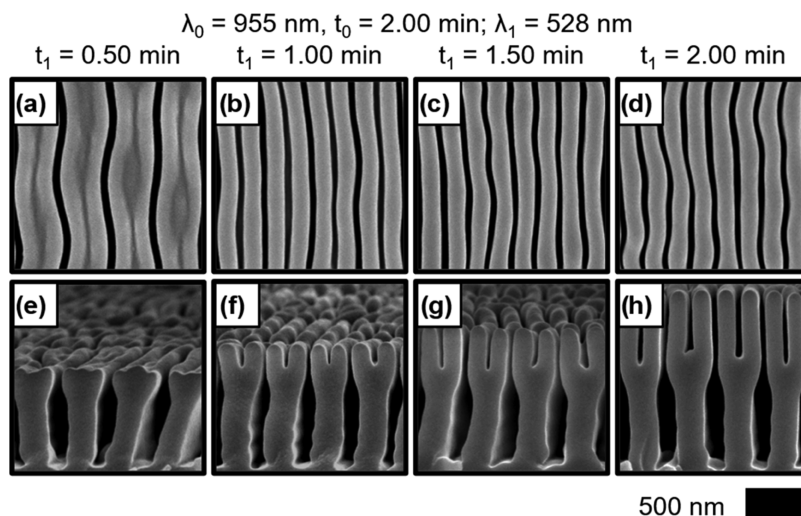


Figure 4. (a–d) Representative top-view and (e–h) cross-sectional SEMs of films generated initially using $\lambda_0 = 955 \text{ nm}$ for $t_0 = 2.00 \text{ min}$ and then extended in a subsequent deposition step using $\lambda_1 = 528 \text{ nm}$ for the indicated t_1 .

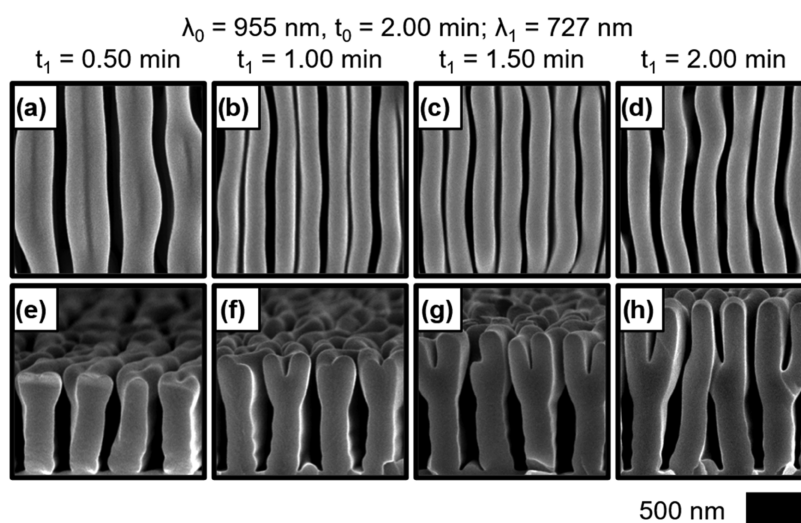


Figure 5. (a–d) Representative top-view and (e–h) cross-sectional SEMs of films generated initially using $\lambda_0 = 955 \text{ nm}$ for $t_0 = 2.00 \text{ min}$ and then extended in a subsequent deposition step using $\lambda_1 = 727 \text{ nm}$ for the indicated t_1 .

anisotropy in the out-of-plane direction. Energy-dispersive X-ray (EDX) spectroscopic analysis indicated that Se–Te films exhibited a Se:Te atomic ratio of approximately 1:2.5.

Figure 2 presents representative top-view (Figure 2a–d) and cross-sectional (Figure 2e–h) SEMs of films that were initially deposited for $t_0 = 2.00 \text{ min}$ using $\lambda_{\text{avg}} = \lambda_0 = 528 \text{ nm}$ illumination (Λ_{528}) and were subsequently extended using $\lambda_{\text{avg}} = \lambda_1 = 955 \text{ nm}$ illumination for the indicated time, t_1 . At $t_1 = 0.50 \text{ min}$, an increased feature width was observed (Figure 2a) relative to that for Λ_{528} films (Figure 1a). Near the tips of the lamellae, deposition occurred in the space between adjoining lamellae, bridging some features (Figure 2e). Further deposition using λ_1 resulted in nonuniform feature heights (Figure 2b); cross-sectional analysis revealed an oscillatory height profile in which approximately every other lamella was extended along the substrate normal, but the interspersed features exhibited little growth (Figure 2f). At $t_1 = 1.50 \text{ min}$, the top-view SEM data revealed a substantial decrease in the interfacial feature density and a concomitant increase in the width of the remaining features (Figure 2c). The cross-

sectional SEM data showed the termination of every second feature defined by the initial deposition with λ_0 (Figure 2g). 2D FT analysis indicated that the pitch of the growing structures increased from $262 \pm 10 \text{ nm}$ for $t_1 = 1.00 \text{ min}$ to $316 \pm 12 \text{ nm}$ for $t_1 = 1.50 \text{ min}$. Additional deposition using $\lambda_1 = 955 \text{ nm}$ resulted in an extension of the remaining features along the substrate normal axis (Figure 2d,h) and a pitch of $361 \pm 6 \text{ nm}$ was measured for $t_1 = 2.00 \text{ min}$, consistent with the pitch observed for Λ_{955} films.

Figure 3 presents representative top-view (Figure 3a–d) and cross-sectional (Figure 3e–h) SEMs of Λ_{727} films that were extended in a second deposition step using $\lambda_1 = 955 \text{ nm}$ for the indicated t_1 . After the input wavelength was changed, a larger interfacial feature width was observed (Figure 3a) relative to that for Λ_{727} films (Figure 1b). Cross-sectional analysis revealed that some features exhibited shorter heights than others (Figure 3e). At $t_1 = 1.00 \text{ min}$, a decrease in the in-plane feature density was observed (Figure 3b) and 2D FT analysis indicated a pitch of $301 \pm 6 \text{ nm}$. Cross-sectional analysis showed that some lamellae had terminated whereas others

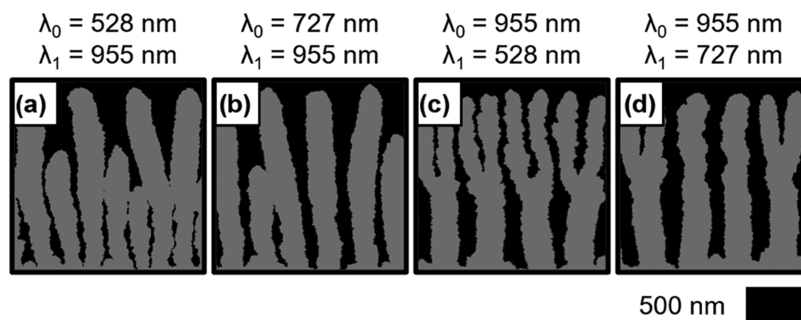


Figure 6. Simulated film morphologies generated first using the indicated λ_0 illumination and then extended using the indicated λ_1 illumination.

continued to grow linearly along the substrate normal (Figure 3f). Additional deposition using $\lambda_1 = 955 \text{ nm}$ led to further decreases in the in-plane feature density (Figure 3c,d), and the pitch increased from $313 \pm 6 \text{ nm}$ at $t_1 = 1.50 \text{ min}$ to $331 \pm 6 \text{ nm}$ at $t_1 = 2.00 \text{ min}$. Additional attenuation of features was observed during this stage of growth, and the lamellae that were next to the sites of terminated growth transiently grew in a direction that was away from the substrate normal and toward the attenuated features and then again grew along the normal (Figure 3g,h). Further deposition using $\lambda_1 = 955 \text{ nm}$ effected continued film evolution in a similar manner, and a pitch of $370 \pm 6 \text{ nm}$ was measured at $t_1 = 3.50 \text{ min}$ (Figure S3), quantitatively matching that measured for Λ_{955} films.

Figure 4 presents representative top-view (Figure 4a–d) and cross-sectional (Figure 4e–h) SEMs of Λ_{955} films that were extended in a second deposition step using $\lambda_1 = 528 \text{ nm}$ illumination for the indicated t_1 . Initial growth with λ_1 produced sets of three parallel bands consisting of two bright bands with a single darker band in between each pair of bright bands (Figure 4a), suggestive of the formation of two new features on top of each preexisting lamella. 2D FT analysis indicated a pitch of $372 \pm 6 \text{ nm}$ at $t_1 = 0.50 \text{ min}$, corresponding to the larger features defined by λ_0 (955 nm). The pitch of the smaller incipient features was $189 \pm 6 \text{ nm}$, as measured by additional 2D FT analysis of the same SEM data but with contrast thresholding applied. The structure with the $189 \pm 6 \text{ nm}$ pitch became predominant (Figure 4b) when the deposition was continued using $\lambda_1 = 528 \text{ nm}$. For $t_1 = 1.00 \text{ min}$, the interfacial morphology appeared similar to that observed for Λ_{528} films (Figure 1a), with a single pitch of $189 \pm 6 \text{ nm}$ at the interface. Qualitatively similar interfacial morphologies were observed for $t_1 = 1.50$ and 2.00 min (Figure 4c,d), with pitches of 190 ± 6 and $197 \pm 6 \text{ nm}$ measured at $t_1 = 1.50$ and at $t_1 = 2.00 \text{ min}$, respectively. Additional growth of the structure to $t_1 = 3.00 \text{ min}$ resulted in a pitch of $204 \pm 6 \text{ nm}$ (Figure S5), consistent with that measured for Λ_{528} films. Cross-sectional SEM analysis revealed the initial generation of two small features that projected outward from each larger underlying feature (Figure 4e); the addition of new mass then extended these features along the substrate normal (Figure 4f–h).

Figure 5 presents representative top-view (Figure 5a–d) and cross-sectional (Figure 5e–h) SEMs of Λ_{955} films extended in a second deposition step using $\lambda_1 = 727 \text{ nm}$ illumination for the indicated t_1 . At $t_1 = 0.50 \text{ min}$, an increase in the interfacial width of the features was observed relative to Λ_{955} films (Figure 1c). A dark band was also observed along the lamellar centerlines with two brighter regions on either side. This observation was indicative of two incipient features on top of

each preexisting feature (Figure 5a,e), similar to the behavior observed for extended growth of Λ_{955} films using $\lambda_1 = 528 \text{ nm}$ (Figure 4). Deposition using $\lambda_1 = 727 \text{ nm}$ for $t_1 = 1.00 \text{ min}$ resulted in further definition of the smaller incipient features and yielded ordered pairs of lamellae (Figure 5b) with widths more similar to those observed for Λ_{727} films (Figure 1b) than for Λ_{955} films (Figure 1c). At this stage of growth, 2D FT analysis revealed two pitches at the interface, $220 \pm 8 \text{ nm}$, corresponding to the individual features at the interface, and $383 \pm 8 \text{ nm}$, corresponding to the pairs of features. Additional deposition with λ_1 resulted in a loss of pairwise order and a decrease in the density of the individual lamellae (Figure 5c,d). A single pitch of $254 \pm 8 \text{ nm}$ was measured for $t_1 = 1.50 \text{ min}$, and this value increased to $272 \pm 14 \text{ nm}$ at $t_1 = 2.00 \text{ min}$, in accord with that observed for Λ_{727} films (Figure 1b). Cross-sectional analysis revealed that two new features were initially generated on top of most preexisting lamellae, although some preexisting features primarily exhibited an increase in width (Figure 5e,f). Upon additional deposition, some features continued to grow linearly along the substrate normal, but others terminated and some exhibited transient growth away from the substrate normal and subsequently fused with a neighboring feature (Figure 5g,h).

The film growth by light-mediated electrodeposition was simulated using an optically based, two-step iterative modeling approach. Full-wave electromagnetic simulations were first performed to calculate the spatially resolved light absorption magnitude. Mass was then added using a Monte Carlo method in which the local probability of addition was weighted by the previously calculated local absorption. These steps were then successively iterated. Empirical inputs to the model were limited to estimates of the complex refractive index of the deposited Se–Te material and the refractive index of the electrolyte. Figure 6 presents simulated film morphologies generated by first modeling the initial deposition using the indicated λ_0 and then modeling extended growth using the indicated λ_1 . The pairs of λ_0 and λ_1 values used in the modeling were equivalent to those investigated experimentally (Figures 2–5). The simulated film morphologies closely matched the analogous experimental data (Figures 2h, 3h, 4h, and 5h), with lamellar features generated in each case with pitches that varied along the substrate normal. The pitch at the interface increased when $\lambda_1 > \lambda_0$ (Figure 6a,b) and decreased when $\lambda_1 < \lambda_0$ (Figure 6c,d).

A series of electromagnetic simulations using simplified morphologies was performed to gain insight into the optical phenomena associated with growth using sequential wavelength inputs. Uniform, idealized lamellar structures were designed with dimensions derived from the experimental data.

Figure 7a,b presents spatial profiles of the time-averaged E-field magnitude, wherein red represents maximal magnitude and

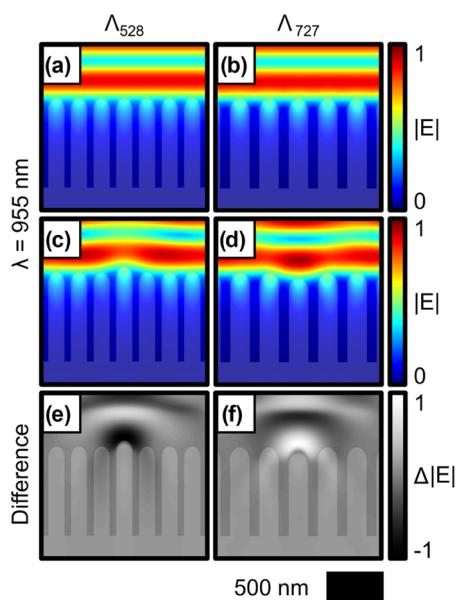


Figure 7. (a, b) Simulated spatial profiles representing the normalized time-averaged E-field magnitude, $|E|$, resulting from $\lambda = 955$ nm illumination of simplified structures representative of the indicated experimentally observed structures. (c, d) Same as (a, b), respectively, but with the height of a single feature adjusted to model initial extension using λ_1 . (e, f) Profiles representing the difference between the magnitudes, $\Delta|E|$, presented in (a, c) and (b, d), respectively.

blue minimal, for illumination with $\lambda = 955$ nm of simulated structures representative of Λ_{528} and Λ_{727} , respectively. In both cases, the profile was isotropic in the direction of feature periodicity above the growth interface. Spatially symmetrical resonances of elevated intensity were observed within each feature tip. These resonances were isotropic within, and equivalent for, all observed features. An additional set of simulations was performed in which the idealized structures were modified to include some height anisotropy, in analogy to the experimentally observed structural evolution following a change in the optical input wavelength from λ_0 to λ_1 with $\lambda_1 > \lambda_0$ (Figures 2 and 3). Figure 7c,d presents data analogous to that in Figure 7a,b but for structures modified to include a single taller (Figure 7c) or shorter (Figure 7d) feature (Figure S8a,b presents analogous data to that in Figure 7a,b but for structures that were modified to include a single shorter [Figure S8a] or taller [Figure S8b] feature). Figure 7e presents the difference between the spatial profiles of E-field magnitude depicted in Figure 7a,c, highlighting the effects of modification of the feature height. This magnitude difference is presented in grayscale for clarity, with white and black indicating increased and decreased magnitude, respectively. The E-field magnitude increased within the taller feature but decreased within and above the features immediately adjacent to the taller structure. Figure 7f presents the difference in the spatial profiles of E-field magnitude depicted in Figure 7b,d. An arc of increased field magnitude was observed above and surrounding the shorter feature and intersecting the neighboring features. Beyond this arc, another arc of decreased field magnitude was observed, with edges that were not localized to a single feature but instead occurred between the first and second nearest

neighbors relative to the central feature. The nearest-neighbor features were consequently presented with an increased field magnitude on the side nearer to the shorter structure and a decreased field magnitude on the side opposite to the shorter structure.

Figure 8a,b presents spatial profiles of the time-averaged E-field magnitude for illumination of a simplified structure

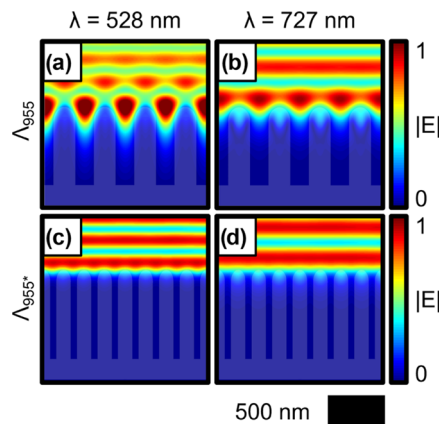


Figure 8. (a, b) Simulated spatial profiles representing the normalized time-averaged E-field magnitude, $|E|$, resulting from illumination with the indicated wavelength of simplified structures representative of the experimentally observed Λ_{955} structure. (c, d) Same as (a, b), respectively, but for simplified Λ_{955^*} structures, in which the pitch was half of that measured for Λ_{955} .

representative of Λ_{955} films with $\lambda = 528$ and 727 nm, respectively. The profiles both exhibited well-defined, intense maxima between the feature tips in addition to local minima directly above each feature. However, for $\lambda = 727$ nm (Figure 8b), the maxima between feature tips were less intense and a larger magnitude was observed at the minima above each feature than for $\lambda = 528$ nm (Figure 8a). To examine the operative optical processes at a subsequent stage of structural evolution, in which growth with λ_1 approximately doubled the interfacial feature density (Figures 4f and 5f), simulations were performed using another set of simplified structures. Figure 8c,d presents data analogous to that in Figure 8a,b but for structures with a feature pitch that was half that observed for Λ_{955} films, denoted as Λ_{955^*} . The E-field magnitude resulting from illumination of the Λ_{955^*} structure was similar with either $\lambda = 528$ nm or $\lambda = 727$ nm, and in both cases, the profile was isotropic in the direction of the feature periodicity above the growth interface.

DISCUSSION

The correlation between the input wavelength and the feature pitch observed for depositions performed using a single illumination input (Figure 1) supports the notion that phenotype plasticity is observed during inorganic phototropic growth. Consistently, unique interfacial structures with discrete pitches are spontaneously generated for discrete, static values of λ_{avg} .¹⁴ Depositions performed using two distinct, sequential illumination inputs, wherein $\lambda_1 > \lambda_0$, exhibited termination of some features along the growth axis after the change in input wavelength. The feature pitch at the interface also monotonically increased (Figures 2 and 3) and eventually matched that observed for deposition using λ_1 alone (Figure 1c,f). These results demonstrate a plastic response to a temporally abrupt

illumination change in a manner analogous to shade-avoiding plants, which exhibit apical dominance (preeminence of the main stem and corresponding suppression of axillary branches) upon encountering far-red illumination.^{8,19,20} Moreover, despite the minimal use of empirical inputs in the modeling, the simulated morphologies (Figure 6a,b) closely matched those observed experimentally for extended growth of Λ_{528} and Λ_{727} structures using $\lambda_1 = 955$ nm (Figures 2h and 3h). This agreement suggests that the structural evolution in response to an increase in the input wavelength is primarily directed by light–material interactions at the growth interface. The operative optical mechanism is illustrated by the associated set of simulations using simplified structures (Figure 7). Illumination of simplified Λ_{528} and Λ_{727} structures with $\lambda_1 = 955$ nm indicated no notable anisotropy in the spatial profile of the E-field magnitude (Figure 7a,b). This result is consistent with the relatively small feature size and pitch relative to the input wavelength ($\lambda_1 = 955$ nm), as well as the lower material absorption coefficient at 955 nm relative to shorter wavelengths, limiting scattering and coupling. These results are suggestive of continued linear extension of all preexisting features. However, stochastic variations in the growth rate of individual features may result in transitory structural anisotropy at the interface. In the case of resonant illumination, ordered growth that maintains isotropic feature sizes is a consequence of cooperative light scattering among neighboring features promoting synergistic light absorption.¹⁷ Here, the mismatch between the illumination wavelength ($\lambda_1 = 955$ nm) and the structure (Λ_{528} and Λ_{727}) can effect scattering that enables positive reinforcement, rather than suppression, of transitory anisotropy and consequently results in structural evolution. The profiles of the E-field magnitude for simplified Λ_{528} and Λ_{727} structures that included a feature with modified height illuminated with $\lambda_1 = 955$ nm (Figure 7c,d) are consistent with this conceptual framework. Similar results were observed when the modified model feature was considered with decreased or increased height (Figures 7c,d and S8a,b). When height asymmetry was present between neighboring features, the tips of taller features exhibited increased E-field magnitude, whereas the tips of shorter features exhibited decreased E-field magnitude, relative to the behavior observed when neighboring features had mutually identical heights (Figure 7a,b). This observation is consistent with the experimental results in which taller features exhibited extended growth, but the growth of shorter features was terminated. In this regard, the characteristics of inorganic phototropic growth resemble the asymmetric competition behavior exhibited by plants in which larger individuals often obtain a disproportionate share of contested resources and suppress the growth of smaller neighbors.^{21,22} Notably, the increase in interfacial magnitude at the taller features in the Λ_{727} structure case was asymmetric, with a larger increase at the side adjacent to the shorter feature. This behavior is consistent with the experimental data in which transient off-normal growth of nearest-neighbor features was observed to proceed toward a terminating feature (Figure 3). This behavior occurs because the Λ_{727} structure pitch is not close to an integral fraction of the Λ_{955} structure pitch, unlike the situation for the Λ_{528} structure. Scattering of the illumination thus results in maximal E-field modulation between, rather than at, preexisting features. Moreover, the near integral relation between the pitches of the Λ_{955} and Λ_{528} films results in an oscillatory feature height profile during extension of a Λ_{528} film with $\lambda_1 =$

955 nm (Figure 2f), whereas no such profile was observed for extension of a Λ_{727} film (Figure 3e–h).

Depositions performed using two distinct, sequential illumination inputs, wherein $\lambda_1 < \lambda_0$, (Figures 4 and 5) exhibited a progressive evolution of the feature pitch at the interface after the input wavelength was changed. Moreover, the pitch decreased as the growth continued and eventually matched that observed for structures generated by growth solely using λ_1 excitation (Figure 1a,b). This process was characterized by a branching phenomenon in which individual preexisting features split along the long in-plane axis, parallel to the input polarization, resulting in pairs of smaller features at the interface that then were subject to further evolution and growth. This result provides an additional demonstration of morphological plasticity in response to an abrupt change in input wavelength. This behavior is analogous to the response exhibited by shade-intolerant plants that initiate branching and laterally increase the density of light-gathering organs upon encountering shorter wavelength light after exposure to far-red illumination.^{19,23} The simulated morphologies for Λ_{955} structures extended using $\lambda_1 = 528$ or 727 nm illumination (Figure 6c,d) closely resembled those generated experimentally (Figures 4h and 5h). This agreement between the computational and experimental data indicates the growth evolution was optically controlled, as noted previously for the case of multistep growth using $\lambda_1 > \lambda_0$. The operative optical mechanism is again demonstrated by the associated set of simulations using simplified structures (Figure 8). Illumination of simplified Λ_{955} structures with $\lambda_1 = 528$ or 727 nm revealed strong maxima in the E-field near the growth interface in the regions between feature tips, which can direct branching growth. These computational data are consistent with the empirical data, wherein the branching of most preexisting features generated two new features from each original feature (Figures 4a,e and 5a,e). FT analysis indicated that this process initially decreased the pitch at the interface rapidly to a value lower not only than that observed for Λ_{955} films but also lower than that for films generated with the respective λ_1 input alone (Λ_{528} or Λ_{727}). Additional growth using $\lambda_1 = 528$ or 727 nm then effected a gradual increase in the pitch until it was in accord with that for Λ_{528} or Λ_{727} films, respectively. This later increase in the pitch was associated with the termination of individual features in a manner analogous to that observed for deposition using sequential inputs with $\lambda_1 > \lambda_0$. Mechanistically, the similarity between these processes is illustrated by the simulations using a simplified structure, Λ_{955}^* , that was designed to model pairwise splitting by setting a pitch equal to half the feature pitch of Λ_{955} films. For illumination with both $\lambda_1 = 528$ nm and $\lambda_1 = 727$ nm (Figure 8c,d), the E-field magnitude showed little spatial anisotropy, reflective of the results observed for illumination of idealized Λ_{528} and Λ_{727} structures with $\lambda_1 = 955$ nm (Figure 7a,b). The termination process was more qualitatively apparent for $\lambda_1 = 727$ nm than for $\lambda_1 = 528$ nm because there was a greater dimensional mismatch between the Λ_{727} structure and the structure generated by pairwise branching of the Λ_{955} structure relative to the mismatch between the latter and the Λ_{528} structure.

For the full the series of input pairs (λ_0, λ_1) explored herein, the two-step deposition process using sequential illumination inputs with $\lambda_0 \neq \lambda_1$ exhibited complete morphological plasticity, in that the resulting interfacial structure was equivalent to that observed for growth solely using λ_1 in a single step. Figures S6 and S7 present graphical flowcharts that

summarize these morphological responses as a function of input wavelength and time for $\lambda_1 > \lambda_0$ and for $\lambda_1 < \lambda_0$, respectively. The plastic nature of the response did not exhibit a history effect, in that the interfacial structure that formed did not critically depend on λ_0 nor on the morphology of the previously defined structure but rather was defined only by λ_1 .¹⁸ This is consistent with the E-field anisotropies demonstrated in the simulations using simplified model structures and suggests that the morphologies defined by λ_0 cannot effectively couple with and accommodate the λ_1 illumination. The observations instead indicate an emergent nanophotonic behavior that directs the structural evolution to generate a feature pitch proportional to λ_1 .^{14,17} The observation of a history effect is thus limited to cases in which a structure, defined by λ_0 , can effectively couple optically with λ_1 (i.e., the scattering by the structure effectively leads to resonant absorption of the illumination). Additionally, the lack of a history effect for input pairs with the order λ_0 , λ_1 and also λ_1 , λ_0 suggests that repeated changes between two inputs should allow for predetermined modulation of the in-plane structure along the growth direction. The cumulative responsive morphological plasticity of structures evolving via inorganic phototropic growth to changes in λ , wherein each new input is physically recorded, indicates that appropriate temporal manipulation of the illumination may enable fabrication of tailored mesostructures with significant three-dimensional intricacy via a continuous growth process. Such structures may be useful in a variety of photonic, fluidic, and electrochemical applications.^{24–26}

CONCLUSIONS

Se–Te films generated by light-mediated electrodeposition using linearly polarized illumination from a single narrowband LED source generated ordered, anisotropic mesostructures with nanoscale lamellar features that projected along the substrate normal and pitches that were proportional to the input wavelength. Films initially generated using a single wavelength input, λ_0 , and extended in a subsequent deposition step with a discrete input, λ_1 , produced a spontaneous plastic response that eventually resulted in an interfacial morphology matching that observed for films generated using λ_1 alone. This structural evolution involved feature termination, branching, and fusion along the growth direction. This adaptive change in the morphology of new growth is analogous to the plastic behavior of plant branches and leaves in response to changes in environmental light conditions. Moreover, such evolution demonstrates the generation of complex morphologies in three dimensions using a single, continuous growth process via only temporal manipulation of the input illumination characteristics. Simulated film morphologies generated using a fully optically based model closely reproduced the morphologies observed experimentally for multistep growth with sequential wavelength inputs, indicating that the plastic response was directed by photonic phenomena at the growth interface. For the cases investigated, deposition using sequential inputs with $\lambda_1 > \lambda_0$ exhibited structural evolution primarily via feature termination. Optical simulations using simplified model structures suggested that this plastic response was directed by interfacial scattering that reinforced stochastically generated nonuniformity in the height of the features. In contrast, explored cases of deposition using sequential inputs with $\lambda_1 < \lambda_0$ initially exhibited pairwise branching of features, decreasing the pitch at the interface to values lower than those

observed for structures generated using either λ_0 or λ_1 alone. Further structural evolution proceeded via feature termination and/or merging of adjacent features. Additional simulations with simplified structures indicated that the initial branching was directed by effective scattering of the shorter λ_1 illumination that produced strong field localization between preexisting features, and subsequent feature density reduction followed a process analogous to that observed for evolution using sequential inputs with $\lambda_1 > \lambda_0$. The cumulative data thus illustrate the capability of inorganic phototropic growth to exhibit morphological plasticity and to adapt to new wavelength inputs via emergent optical self-regulation and demonstrate that structures with complexity in three dimensions, e.g., periodic tuning fork and aqueduct-like structures, can be generated by facile manipulation of only the optical input characteristics.

METHODS

Materials and Chemicals

H₂SO₄ (ACS Reagent, J. T. Baker), buffered HF improved etchant (Transene), SeO₂ (99.4%, Alfa Aesar), and TeO₂ (99+ %, Sigma-Aldrich) were used as received. H₂O with a resistivity ≥ 18.2 M Ω cm (Barnstead Nanopure System) was used throughout. n⁺-Si(100) (<0.005 Ω cm, As-doped, 525 \pm 25 μ m, single-side polished, Addison Engineering) was coated with Au as noted in the subheading below (Substrate Preparation) and used as a substrate for deposition. Flash-dry Ag paint (SPI Supplies), EP21ARHTND epoxy (MasterBond), and nitrocellulose-based nail polish were used to assemble the working electrodes.

Substrate Preparation

n⁺-Si wafers were etched with buffered HF(aq) for 30 s, rinsed with H₂O, dried under a stream of N₂(g), and then immediately transferred to an electron-beam metal evaporator with a base pressure <10⁻⁶ torr. Using an accelerating voltage of 10 kV, a 10 nm Ti adhesion layer was deposited on the polished side of the wafer using a 40 mA deposition current, and then 50 nm of Au was deposited on top of the Ti using a 150 mA deposition current. 20 nm of Ti was deposited on the unpolished side of the wafer to serve as a back contact. The Au-topped Si sections were then cut into square 0.50 cm by 0.50 cm sections for use as deposition substrates.

Electrode Preparation

To prepare electrode assemblies, two Al half-round bars with a 0.25" diameter and 4" in length were joined together with epoxy at the flat sides with an \sim 0.4" offset in the long dimension to form a cylinder with two half-round ends. Poly(tetrafluoroethylene) heat-shrink tubing was applied over the cylinder to insulate the cylindrical region from the solution. The rounded side of one of the half-round ends was insulated with epoxy. Ag paint was used to affix a Au-topped Si section with a Ti-coated back surface to the flat side of the epoxy-insulated half-round end. Nail polish was used to insulate the remaining uncovered area on the flat surface that surrounded the Au-topped Si section. Figure S9 presents a schematic of an electrode assembly with an attached Au-topped Si section. Immediately before deposition, the surface of each electrode was briefly cleaned using a stream of N₂(g).

Electrode Illumination

Illumination for photoelectrochemical growth was provided by narrowband diode (LED) sources (Thorlabs) with intensity-weighted average wavelength, λ_{avg} values and spectral bandwidths (FWHM) of 955 and 60 nm (M970L4), 727 and 37 nm (M730L4), and 528 and 32 nm (SOLIS-S25C), respectively. A single aspheric lens (\varnothing 50.8 mm, f = 32 mm) was utilized in conjunction with the λ_{avg} = 955 and 727 nm sources to collect, condense, and collimate the output. To do the same with the λ_{avg} = 528 nm source, a series of three lenses, consisting of an aspheric lens (\varnothing 25.4 mm, f = 16 mm) along with two biconvex lenses (\varnothing 50.8 mm, f = 60 mm and \varnothing 50.8 mm, f = 100 mm)

was utilized. A film polarizer (LPVISE200-A or LPNIRE200-B, Thorlabs) was inserted after the lenses to produce vertical linear polarization. A 1500 grit ground-glass (UV fused silica) diffuser was placed immediately in front of the photoelectrochemical cell to ensure spatial homogeneity of the illumination.

The light intensity incident on the electrode was measured by placing a calibrated Si photodiode (Thorlabs FDS100), instead of an electrode assembly, in the photoelectrochemical cell with electrolyte, and the steady-state current response of that Si photodiode was measured. Depositions with $\lambda_{\text{avg}} = 528, 727, \text{ and } 955 \text{ nm}$ were performed with light intensities of 38, 56, and 123 mW cm^{-2} , respectively.

Photoelectrochemical Deposition

Photoelectrochemical deposition was performed using a Bio-Logic SP-200 potentiostat. The deposition was performed in a two-compartment glass cell with a quartz window. A three-electrode configuration was utilized with a Ag/AgCl reference electrode (3.00 M KCl, Bioanalytical Systems) and an Ir wire counter electrode (99.999%, Sigma-Aldrich) isolated behind a porous glass frit. The counter electrode was separated from the main compartment to minimize contamination of the deposition substrate by any potential corrosion products or other species in the anolyte chamber. Films were deposited from an aqueous solution of 0.0200 M SeO_2 , 0.0100 M TeO_2 , and 2.00 M H_2SO_4 . The deposition was effected by supplying under galvanostatic control a current density of -8.00 mA cm^{-2} to the Au-coated electrode for 2.00 min, illuminated as detailed under the above subheading (Electrode Illumination). This current demand resulted in an electrode potential of approximately $-0.12 \pm 0.03 \text{ V}$ vs Ag/AgCl for all illumination conditions used in this work. For depositions using two sequential, discrete illumination inputs, the electrode was transiently floated to open circuit following initial deposition as the illumination input was changed, and deposition was then continued with the new illumination input by supplying -8.00 mA cm^{-2} under galvanostatic control for an additional 0.50–2.00 min (unless otherwise noted). Figure S10 presents an experimental schematic for such growth using sequential, discrete spectral inputs. After deposition, the electrode was immediately removed from the cell, rinsed with H_2O , and dried under a stream of $\text{N}_2(\text{g})$. The Au-coated substrate with top-facing Se–Te film was mechanically separated from the rest of the electrode assembly. The nitrocellulose-based insulation and the majority of the Ag paint were then removed mechanically.

Microscopy

Scanning electron micrographs (SEMs) were obtained with an FEI Nova NanoSEM 450 at an accelerating voltage of 5.00 kV with a working distance of 5 mm and an in-lens secondary electron detector. Micrographs obtained for quantitative analysis were acquired with a resolution of 172 pixels μm^{-1} over $\sim 120 \mu\text{m}^2$ areas. Micrographs that were used to produce display figures were acquired with a resolution of 344 pixels μm^{-1} over $\sim 2 \mu\text{m}^2$ areas.

Simulation of Film Morphology

The growths of the photoelectrochemically deposited films were simulated with an iterative growth model in which electromagnetic simulations were first used to calculate the local photocarrier-generation rates at the film surface. Then, mass addition was simulated via a Monte Carlo method in which the local photocarrier-generation rate weighted the local rate of mass addition along the film surface.

Growth simulations began with a bare, semi-infinite planar substrate. In the first step, the light-absorption profile under a linearly polarized, plane-wave illumination source was calculated using full-wave finite-difference time-domain (FDTD) simulations (“FDTD Solutions” software package, Lumerical) with periodic boundary conditions along the substrate interface. In the second step, a Monte Carlo simulation was performed in which an amount of mass, equaling that of a 5 nm planar layer covering the simulation area, was added to the upper surface of the structure with a probability F

$$F(G) = G \prod_{i=1}^3 \frac{x_i}{r_i} \quad (1)$$

where G is the spatially dependent photocarrier-generation rate at the film/solution interface, x_i is the fraction of i th nearest neighbors occupied in the cubic lattice, and r_i is the distance to the i th nearest neighbor. The multiplicative sum in the definition of this probability (eq 1) serves to reduce the surface roughness of the film to mimic that observed experimentally. After the initial Monte Carlo simulation, the absorbance of the new, structured film was then calculated in the same manner as for the initial planar film, and an additional Monte Carlo simulation of mass addition was performed. This process of absorbance calculation and mass addition was repeated until the simulated morphologies had heights equivalent to those exhibited by the experimentally generated deposits. To model growth using two sequential, discrete illumination inputs, the computational process was first iterated using the initial illumination input until the simulated morphology height was equivalent to the heights observed for the experimentally generated films using that initial input. The simulated illumination was then updated to represent the new optical input, and the computational process was further iterated until the simulated morphologies had heights equivalent to those exhibited by the experimentally generated films for growth with sequential, discrete illumination inputs.

Experimentally measured values of the wavelength-dependent complex refractive index of Se–Te were utilized. A value of $n = 1.33$ was used for the refractive index of the electrolyte, regardless of wavelength.²⁷ Simulations of the film morphology utilized the intensity-weighted average wavelengths, λ_{avg} , of the experimental sources described above in the Electrode Illumination subheading. A two-dimensional square mesh with a lattice constant of 5 nm was used for the simulations.

Electromagnetic Simulations Using Simplified Structures

Two-dimensional FDTD simulations were used to calculate the time-averaged E-field magnitude for illumination of idealized structures. Structures were designed with dimensions derived from experimental data. The same index data used for the growth modeling were utilized here. The E-field vector of the illumination was oriented parallel to the substrate. A square simulation mesh was used with a lattice constant of 2 nm. Perfectly matched layer boundary conditions were imposed in the direction parallel to the propagation direction, whereas periodic boundary conditions were imposed in the perpendicular direction.

■ ASSOCIATED CONTENT

Supporting Information

The Supporting Information is available free of charge at <https://pubs.acs.org/doi/10.1021/jacsau.1c00588>.

Two-dimensional Fourier transform data, additional scanning electron micrographs, flowcharts graphically summarizing deposit morphological evolution, additional simulations, electrode assembly schematic, experimental schematic, energy-dispersive X-ray spectroscopy data, X-ray diffraction data, complex refractive index data, and average LED emission wavelength data (PDF)

■ AUTHOR INFORMATION

Corresponding Authors

Nathan S. Lewis – Division of Chemistry and Chemical Engineering, California Institute of Technology, Pasadena, California 91125, United States; Beckman Institute, California Institute of Technology, Pasadena, California 91125, United States; orcid.org/0000-0001-5245-0538; Email: nslewis@caltech.edu

Azhar I. Carim — Division of Chemistry and Chemical Engineering, California Institute of Technology, Pasadena, California 91125, United States; Beckman Institute, California Institute of Technology, Pasadena, California 91125, United States; orcid.org/0000-0003-3630-6872; Email: aic@caltech.edu

Authors

Kathryn R. Hamann — Division of Chemistry and Chemical Engineering, California Institute of Technology, Pasadena, California 91125, United States; orcid.org/0000-0003-1163-7173

Madeline C. Meier — Division of Chemistry and Chemical Engineering, California Institute of Technology, Pasadena, California 91125, United States; orcid.org/0000-0003-1608-0810

Complete contact information is available at:
<https://pubs.acs.org/10.1021/jacsau.1c00588>

Notes

The authors declare no competing financial interest.

ACKNOWLEDGMENTS

This work was supported by the National Science Foundation, Directorate for Mathematical & Physical Sciences, Division of Materials Research under Award No. DMR-1905963. The authors gratefully acknowledge J.R. Thompson for insightful discussions, E.D. Simonoff and S. Yalamanchili for assistance with substrate preparation, and R. Gerhart, N. Hart, and B. Markowicz for assistance with photoelectrochemical cell fabrication. KRH and MCM acknowledge Graduate Research Fellowships from the National Science Foundation. MCM also acknowledges the Resnick Institute at Caltech for fellowship support.

REFERENCES

- (1) Agrawal, A. A. Phenotypic Plasticity in the Interactions and Evolution of Species. *Science* **2001**, *294*, 321–326.
- (2) Satbhai, S. B.; Ristova, D.; Busch, W. Underground tuning: quantitative regulation of root growth. *J. Exp. Bot.* **2015**, *66*, 1099–1112.
- (3) Hutchings, M. J.; de Kroon, H. Foraging in Plants: the Role of Morphological Plasticity in Resource Acquisition. In *Advances in Ecological Research*; Begon, M.; Fitter, A. H., Eds.; Academic Press: London, 1994; Vol. 25, pp 159–238.
- (4) Mou, P.; Jones, R. H.; Tan, Z.; Bao, Z.; Chen, H. Morphological and physiological plasticity of plant roots when nutrients are both spatially and temporally heterogeneous. *Plant Soil* **2013**, *364*, 373–384.
- (5) de Wit, M.; Pierik, R. Photomorphogenesis and Photoreceptors. In *Canopy Photosynthesis: From Basics to Applications*; Hikosaka, K.; Niinemets, Ü.; Anten, N. P. R., Eds.; Springer: Netherlands, 2016; Vol. 42, pp 171–186.
- (6) Christie, J. M.; Murphy, A. S. Shoot phototropism in higher plants: New light through old concepts. *Am. J. Bot.* **2013**, *100*, 35–46.
- (7) Ballaré, C. L.; Scopel, A. L.; Roush, M. L.; Radosevich, S. R. How plants find light in patchy canopies. A comparison between wild-type and phytochrome-B-deficient mutant plants of cucumber. *Funct. Ecol.* **1995**, *9*, 859–868.
- (8) Arens, N. C.; Baracaldo, P. S. Variation in Tree Fern Stipe Length with Canopy Height: Tracking Preferred Habitat Through Morphological Change. *Am. Fern. J.* **2000**, *90*, 1–15.
- (9) Park, Y.; Runkle, E. S. Far-red radiation promotes growth of seedlings by increasing leaf expansion and whole-plant net assimilation. *Environ. Exp. Bot.* **2017**, *136*, 41–49.
- (10) Meier, M. C.; Cheng, W.-H.; Atwater, H. A.; Lewis, N. S.; Carim, A. I. Inorganic Phototropism in Electrodeposition of Se-Te. *J. Am. Chem. Soc.* **2019**, *141*, 18658–18661.
- (11) Sadtler, B.; Burgos, S. P.; Batara, N. A.; Beardslee, J. A.; Atwater, H. A.; Lewis, N. S. Phototropic growth control of nanoscale pattern formation in photoelectrodeposited Se-Te films. *Proc. Natl. Acad. Sci. U.S.A.* **2013**, *110*, 19707–19712.
- (12) Carim, A. I.; Hamann, K. R.; Batara, N. A.; Thompson, J. R.; Atwater, H. A.; Lewis, N. S. Template-Free Synthesis of Periodic Three-Dimensional PbSe Nanostructures via Photoelectrodeposition. *J. Am. Chem. Soc.* **2018**, *140*, 6536–6539.
- (13) Hamann, K. R.; Carim, A. I.; Meier, M. C.; Thompson, J. R.; Batara, N. A.; Yermolenko, I. S.; Atwater, H. A.; Lewis, N. S. Optically tunable mesoscale CdSe morphologies via inorganic phototropic growth. *J. Mater. Chem. C* **2020**, *8*, 12412–12417.
- (14) Carim, A. I.; Batara, N. A.; Premkumar, A.; Atwater, H. A.; Lewis, N. S. Self-Optimizing Photoelectrochemical Growth of Nanopatterned Se-Te Films in Response to the Spectral Distribution of Incident Illumination. *Nano Lett.* **2015**, *15*, 7071–7076.
- (15) Carim, A. I.; Batara, N. A.; Premkumar, A.; Atwater, H. A.; Lewis, N. S. Polarization Control of Morphological Pattern Orientation During Light-Mediated Synthesis of Nanostructured Se-Te Films. *ACS Nano* **2016**, *10*, 102–111.
- (16) Carim, A. I.; Batara, N. A.; Premkumar, A.; May, R.; Atwater, H. A.; Lewis, N. S. Morphological Expression of the Coherence and Relative Phase of Optical Inputs to the Photoelectrodeposition of Nanopatterned Se-Te Films. *Nano Lett.* **2016**, *16*, 2963–2968.
- (17) Carim, A. I.; Meier, M. C.; Kennedy, K. M.; Richter, M. H.; Hamann, K. R.; Lewis, N. S. Assessing Effects of Near-Field Synergistic Light Absorption on Ordered Inorganic Phototropic Growth. *J. Am. Chem. Soc.* **2021**, *143*, 3693–3696.
- (18) Hamann, K. R.; Carim, A. I.; Meier, M. C.; Lewis, N. S. Path-Dependent Morphological Evolution of Se-Te Mesostructures Prepared by Inorganic Phototropic Growth. *J. Am. Chem. Soc.* **2020**, *142*, 19840–19843.
- (19) Slade, A. J.; Hutchings, M. J. The Effects of Light Intensity on Foraging in the Clonal Herb *Glechoma Hederacea*. *J. Ecol.* **1987**, *75*, 639–650.
- (20) Doebley, J.; Stec, A.; Hubbard, L. The evolution of apical dominance in maize. *Nature* **1997**, *386*, 485–488.
- (21) Schwinning, S.; Weiner, J. Mechanisms Determining the Degree of Size Asymmetry in Competition among Plants. *Oecologia* **1998**, *113*, 447–455.
- (22) Farrior, C. E.; Bohlman, S. A.; Hubbell, S.; Pacala, S. W. Dominance of the suppressed: Power-law size structure in tropical forests. *Science* **2016**, *351*, 155–157.
- (23) Finlayson, S. A.; Krishnareddy, S. R.; Kebrom, T. H.; Casal, J. J. Phytochrome regulation of branching in Arabidopsis. *Plant Physiol.* **2010**, *152*, 1914–1927.
- (24) Vukusic, P.; Sambles, J. R.; Lawrence, C. R. Colour mixing in wing scales of a butterfly. *Nature* **2000**, *404*, 457.
- (25) Zheng, Y.; Gao, X.; Jiang, L. Directional adhesion of superhydrophobic butterfly wings. *Soft Matter* **2007**, *3*, 178–182.
- (26) Chen, Z.; Cummins, D.; Reinecke, B. N.; Clark, E.; Sunkara, M. K.; Jaramillo, T. F. Core-shell MoO₃-MoS₂ Nanowires for Hydrogen Evolution: A Functional Design for Electrocatalytic Materials. *Nano Lett.* **2011**, *11*, 4168–4175.
- (27) Hale, G. M.; Querry, M. R. Optical Constants of Water in the 200-nm to 200- μ m Wavelength Region. *Appl. Opt.* **1973**, *12*, 555–563.